Biosensors and Bioelectronics 191 (2021) 113412

Contents lists available at ScienceDirect

Biosensors and Bioelectronics

journal homepage: www.elsevier.com/locate/bios

Label-free biosensor of phagocytosis for diagnosing bacterial infections

Junchen Liao [a], Jifeng Ren [a,b], Huang Wei [a], Raymond H.W. Lam [a,c,d], Song Lin Chua [e,f,g,**], Bee Luan Khoo [a,*]

[a] Department of Biomedical Engineering, City University of Hong Kong, Hong Kong SAR, China
[b] School of Biomedical Engineering, Capital Medical University, Beijing, 100069, China
[c] City University of Hong Kong Shenzhen Research Institute, Shenzhen, 518057, China
[d] Centre for Robotics and Automation, City University of Hong Kong, Hong Kong SAR, China
[e] Department of Applied Biology and Chemical Technology, The Hong Kong Polytechnic University, Hong Kong SAR, 999077, China
[f] State Key Laboratory of Chemical Biology and Drug Discovery, The Hong Kong Polytechnic University, Hong Kong SAR, 999077, China
[g] Shenzhen Key Laboratory of Food Biological Safety Control, China

ARTICLE INFO

Keywords:
Phagocytosis
Microfluidics
Infections
Diagnosis

ABSTRACT

Phagocytic cells recognize and phagocytose invading microbes for destruction. However, bacterial pathogens can remain hidden at low levels from conventional detection or replicate intracellularly after being phagocytosed by immune cells. Current phagocytosis-detection approaches involve flow cytometry or microscopic search for rare bacteria-internalized phagocytes among large populations of uninfected cells, which poses significant challenges in research and clinical settings. Hence it is imperative to develop a rapid, non-disruptive, and label-free phagocytosis detection approach. Using deformability assays and microscopic imaging, we have demonstrated for the first time that the presence of intracellular bacteria in phagocytic blood cells led to aberrant physical properties. Specifically, human monocytes with internalized bacteria of various species were stiffer and larger compared with uninfected monocytes. Taking advantage of these physical differences, a novel microfluidics-based biosensor platform was developed to passively sort, concentrate and quantify rare monocytes with internalized pathogens (MIP) from uninfected monocyte populations for phagocytosis detection. The clinical utility of the MIP platform was demonstrated by enriching and detecting bacteria-internalized monocytes from spiked human blood samples within 1.5 h. Patient-derived clinical isolates were used to validate the utility of the MIP platform further. This proof-of-concept presents a phagocytosis detection platform that could be used to rapidly diagnose microbial infections, especially in bloodstream infections (BSIs), thereby improving the clinical outcomes for point-of-care management.

1. Introduction

One of the hallmarks of bacterial infection is the phagocytic uptake of pathogens by immune cells for targeted destruction. However, bacteria may either adopt an intracellular lifestyle to evade immune detection or remain hidden in small populations of phagocytes. Due to the technical difficulties in separating rare bacteria-internalized phagocytes from other white blood cells (WBCs), this results in poor detection of early infections. In immunocompromised individuals, such as the elderly, children, and patients with acquired immunodeficiency syndrome or cancer, sudden escalation in disease severity often lead to rapid deterioration, severe complications, and even death if gone undetected (Peters et al., 2004). Furthermore, long-term monitoring involves routine blood culture, polymerase chain reaction, fluorescence *in situ* hybridization, or flow cytometry, requiring hours to days of analysis, leading to reduced diagnostic efficiency (Peker et al., 2018). (Table 1)

Phagocytes often undergo complex cytoskeleton remodeling, membrane trafficking, and cytokine signaling during the formation of pseudopodia and engulfment of pathogens (Masters et al., 2013). While mechanical forces of phagocytes' pseudopods during formation and particle uptake were previously measured (Srivastava et al., 2020; Yap and Kamm, 2005), the overall mechanical effect on phagocytes containing internalized bacteria remains unclear. This also raises a

* Corresponding author.
** Corresponding author. Department of Applied Biology and Chemical Technology, The Hong Kong Polytechnic University, Hong Kong SAR, 999077, China.
E-mail addresses: song-lin.chua@polyu.edu.hk (S.L. Chua), blkhoo@cityu.edu.hk (B.L. Khoo).

https://doi.org/10.1016/j.bios.2021.113412
Received 17 May 2021; Accepted 2 June 2021
Available online 11 June 2021
0956-5663/

significant question if we can harness such mechanical changes after phagocytosis to isolate and concentrate small numbers of bacteria-internalized phagocytes from large populations of host cells, with the ultimate aim of detecting early or intracellular infections rapidly in a label-free manner.

Here, we first demonstrated that human monocytes, after internalizing various bacterial pathogen species, had an overall increase in mass and cell stiffness, using microscopy measurements and a microfluidic-based deformability assay, respectively. There is no prior study conducted to demonstrate a correlation of phagocytic cell stiffness with bacterial phagocytosis to the best of our knowledge.

Leveraging the mechanical differences in bacteria-internalized monocytes and uninfected monocytes, we developed a microfluidic-based biosensor based on inertial focusing to differentially detect low numbers of human monocytes with internalized pathogens (MIP) from large uninfected populations rapidly. By achieving excellent sensitivity with a limit of detection of 1 bacterium to 100 human cells, this proof-of-concept demonstrated a phagocytosis detection platform that enabled us to quantify and detect low infection levels by various bacterial species. The platform was further validated with patient-derived clinical isolates. Quantitative outputs can be obtained within 1.5 h. Overall, we have presented for the first time a point-of-care diagnostic method that exploits the presence of bacteria-internalized phagocytes to detect early disease or intracellular infection. We envisioned that the MIP device platform could be widely applied to other pathogens related to bloodstream infections (BSIs), low-grade or intracellular infections, or to monitor immunocompromised individuals with potential pathogen infections.

2. Results

2.1. Bacteria-internalized monocytes displayed unique physical parameters from uninfected monocytes

To address how the physical properties of phagocytes alter after bacterial phagocytosis, we first evaluated the range of cell sizes obtained from infected and uninfected human monocytes. Next, we used *Pseudomonas aeruginosa* (*P. aeruginosa*) as a classic example to establish an infection model for testing. *P. aeruginosa* is an opportunistic pathogen for immunocompromised individuals (such as the elderly and AIDS patients), where it frequently infects the respiratory tract, urinary tract, burns, wounds, leading to sepsis (Buyck et al., 2013). Though classically named as an extracellular pathogen, increasing evidence had also shown that *P. aeruginosa* could survive intracellularly within host cells and contribute to intracellular infections (Garai et al., 2019; Garcia-Medina et al., 2005).

We demonstrated that the size range of monocytes with internalized bacteria at multiplicity of infection (MOI; bacterium: monocyte) (MOI 10:1) was significantly larger than that of uninfected monocytes (Fig. 1A, Supplementary Figure 1), contributing to the difference in cell focusing within the device channel. However, the size of most infected monocytes (MOI 10:1) still had some overlap with the size of uninfected monocytes, indicating that another physical parameter was also at play. Hence, we examined if infected monocytes could exhibit any variation in their deformability by employing a microfluidic-based deformability assay (Hu et al., 2018). To simulate initial infections with low bacterial count (low infection rates) and full-blown infections with bacterial infection of most cells (high infection rates) (Bedi et al., 2016; Shin et al., 2017), samples infected at a range of MOI (from lowest of 0.1:1 to highest of 10:1) were utilized. Interestingly, we found that infected monocytes were significantly stiffer than uninfected monocytes (Fig. 1B–D). Based on these results, we determined the positive correlation between MOI and monocyte stiffness for the first time via Equation (1) (Supplementary Figure 2):

$$y = 0.95 - 0.139 \ln(x + 0.02593) \quad (1)$$

where 'y' states for cell stiffness and 'x' states for infection rate (MOI).

Overall, the stiffness of cells infected at higher MOIs (0.1:1 to 1:1) was significantly higher than that of cells infected at lower MOIs (0.01:1 to 0.1:1), indicating that the degree of infection was correlated positively to cell stiffness (Fig. 1B).

2.2. Mechanisms of the MIP platform

Drawing from the idea that initial focusing-based microfluidic platforms often capitalize on differences in physical properties for detection (Herrmann et al., 2019; Zhou et al., 2018), we developed the MIP device, which was directed to sort and enrich rare bacteria-infected monocytes from heterogeneous uninfected populations based on the differences in cell size and deformability. This enables us to detect early infection or intracellular infection at high sensitivity and low cost. The MIP device was fabricated using soft lithography methods described elsewhere (Khoo et al., 2019). The device consisted of three components: (i) an inlet for sample inflow, (ii) a main curvilinear channel for cell focusing, and (iii) five outlets for the separation of cells focused at different regions across the channel cross-section (Fig. 2A).

We demonstrated that the stiffer and larger infected monocytes were concentrated in the first three outlets, leading to a lower proportion of cells at the target outlets (Outlets 4–5) (Fig. 2B). The differential cell

Table 1
Comparison of MIP platform with existing technologies.

	Type	Pathogen-type	Time	Cost	Mode of detection	Ref
Culture-based	**Blood culture**	Bacteria	>2 days	Low	Planktonic bacteria	(Peker et al., 2018; Peters et al., 2004)
Gene-based	**Karius test (cfDNA based)**	Bacteria, virus, fungus, etc	24 h–96 h	High	Genes	Blauwkamp et al. (2019)
	Aptamer-Based Recognition	*S. aureus and Escherichia coli*	<2 h	Medium	Planktonic bacteria	Shen et al. (2016)
	Immunoaffinity mass spectrometry	*Escherichia coli, Bacillus subtilis,* and *S. aureus*	12 h	High	Planktonic bacteria	Zhu et al. (2016)
Protein-based	**Enzyme-based immunodetection assay**	SARS-CoV-2	>24 h (MOI ≥ 3:1); >48 h (MOI 1:200)	Medium	Enzymes	Conzelmann et al. (2020)
	Integrated Comprehensive Droplet Digital Detection system	*Escherichia coli*	1.5–4 h	High	Enzymes	Kang et al. (2014)
Physical property-based	**MIP Biosensor for phagocytosis detection**	*P.aeruginosa, S. aureus, S.* Typhimurium, *S. agalactiae, K. pneumoniae,* and patient-derived clinical isolates	<1.5 h (MOI ≥ 0.01 : 1)	Low	Intracellular bacteria	

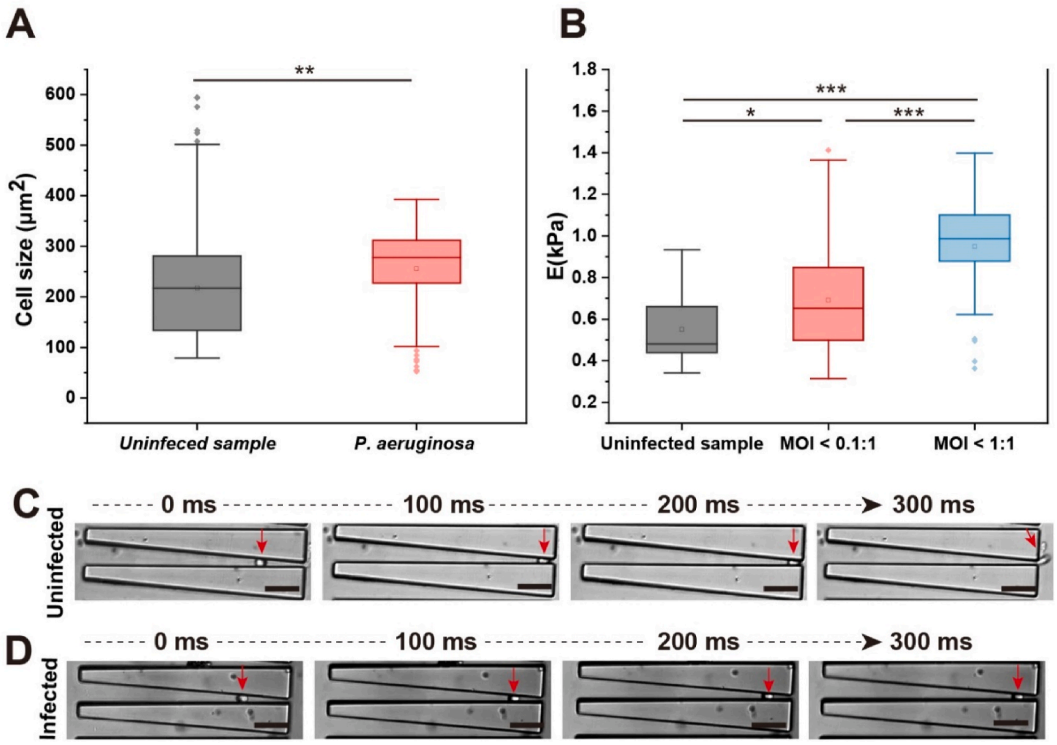

Fig. 1. Stiffness of infected and uninfected monocytes. A) Size range of uninfected and bacteria-infected monocytes. B) Stiffness of uninfected and *P. aeruginosa* infected monocytes at various MOI (Uninfected: 0.55 ± 0.03 kPa; MOI < 0.1:1: 0.69 ± 0.04 kPa; MOI < 1:1: 0.95 ± 0.24 kPa), E(kPa) = Elastic modulus (kilopascals). C) Representative time lapse frames of uninfected monocytes (indicated with red arrow) passing through the device for stiffness measurements. Scale bar = 50 μm. D) Representative time lapse frames of infected monocytes (indicated with red arrow) passing through the device for stiffness measurements. Scale bar: 50 μm * states for p values of <0.01, ** states for p values of <0.001, *** states for p values of <0.0001, ms = millisecond. (For interpretation of the references to colour in this figure legend, the reader is referred to the Web version of this article.)

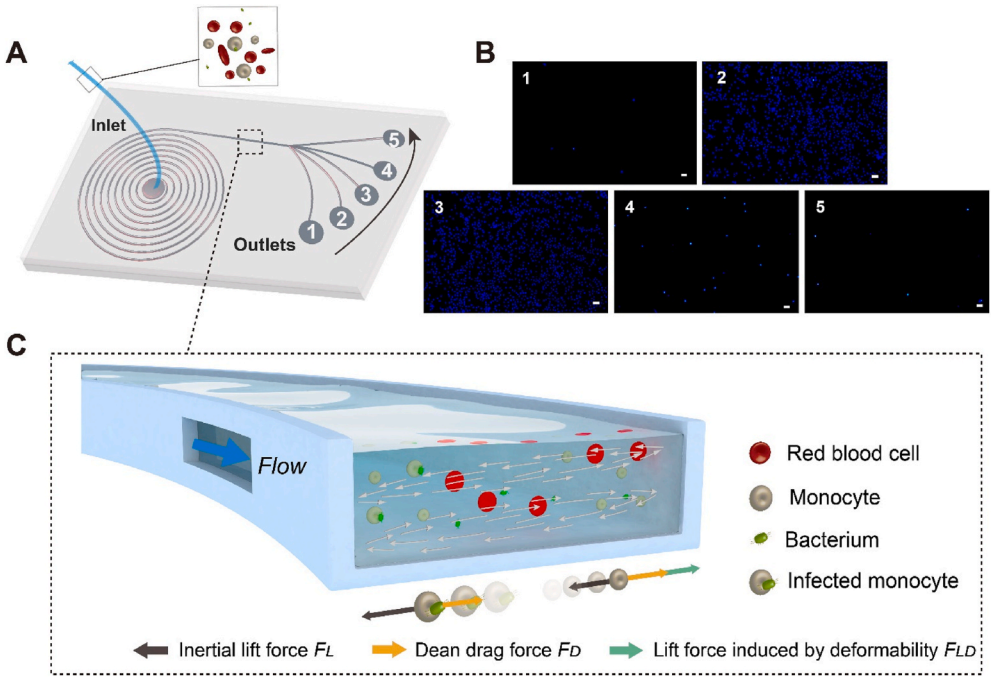

Fig. 2. Label-free microchip to detect monocytes with internalized pathogens (MIP). A)Schematic diagram of the MIP device. Each microchiphad one inlet and five outlets. Samples were introduced through the microchipinlet, and the sorted cells were collected from each outlet, respectively. For blood samples, nucleated cell fractions were processed after red blood cell lysis. B) Representative images of monocytes were collected from each outlet after sorting. The proportion of cells from outlets 2 and 3 were highest due to the higher flow rate. Scale bar: 50 μm. C) Schematic diagram of force distribution within the MIP device. Deformable healthy monocytes experienced an additional lift force and moved close to the outer wall, while stiffer and larger infected cells moved close to the inner wall. (For interpretation of the references to colour in this figure legend, the reader is referred to the Web version of this article.)

separation with the MIP device was realized with the principles of inertial focusing. Briefly, monocytes in the microchip were subjected to two main forces: inertial lift force (F_L) and Dean Drag force (F_D) (Amini et al., 2014; Lim et al., 2014). During device processing, cells would be focused as tightly ordered streams when F_L was balanced with F_D. Thus, larger cells encounter a larger F_L than smaller cells to balance F_D, and the cells would be driven closer to the inner channel wall. Furthermore, deformable cells would experience an additional lift force (F_{LD})

(Guzniczak et al., 2020), pushing cells closer to the outer wall. Therefore, as particles with different sizes and deformability experienced various degrees of F_L at different lateral positions of the channel cross-section, differential focusing of the cells would occur, resulting in efficient separation at the outlets (Fig. 2C) (Gossett et al., 2012; Guzniczak et al., 2020).

2.3. Evaluating the operating parameters of the MIP platform

Next, we aimed to determine the parameters needed to obtain a robust cell proportion threshold in the target outlets, using samples of uninfected monocytes with the MIP platform.

First, we processed various cell concentrations ranging from 0.01 × 10^6 cells ml^{-1} to 2 × 10^6 cells ml^{-1}. Then, we recorded the time-lapse frames of their focused streams in the device to investigate the optimal concentration of monocytes. Before being processed through the channel, the cells were pre-stained with Calcein-AM dyes (Fig. 3A, Supplementary Figure 3A). There was no significant difference in cell diameter for uninfected monocytes (15.51 ± 3.25 μm). In this way, uninfected monocytes were more evenly distributed across the outlets, albeit more cells were concentrated in Outlets 2–3 due to a higher flow rate within these channels (Supplementary Figure 3B). We demonstrated that as the cell concentration increased, the focused cell bandwidth across the channel cross-section would widen (Fig. 3B). Specifically, samples with a cell concentration higher than 1 × 10^6 cells ml^{-1} would result in diffused cell bandwidths of >80 μm, which was wider than the minimum feature size of the MIP device platform, thereby affecting the separation efficiency at the outlets. Therefore, the optimal cell concentration for these samples will be under 1 × 10^6 cells ml^{-1}.

We determined the proportion of uninfected monocytes in the target outlets (Outlets 4–5) of samples with various cell concentrations under 1 × 10^6 cells ml^{-1} (0.033 × 10^6 cells ml^{-1} to 0.166 × 10^6 cells ml^{-1}). We demonstrated that for samples with a cell concentration range of 0.1 × 10^6 cells ml^{-1} to 0.166 × 10^6 cells ml^{-1}, the proportion of cells in the target outlets was consistently higher (8.17–8.71%). Conversely, the proportion of cells in the target outlets was negligible for samples with a cell concentration below 0.1 × 10^6 cells ml^{-1} (2.0–2.86%) (Fig. 3C). Therefore, the optimal range of cell concentration for processing using the MIP device platform was 0.1 × 10^6 cells ml^{-1} to 1 × 10^6 cells ml^{-1}. Due to the advantages of microfluidics, only a small sample volume was required, and the optimal cell concentration of 0.1 × 10^6 cells ml^{-1} was equivalent to 1 ml of blood. A cut-off value of 25 percentile was used to distinguish samples with infected monocytes clearly. Therefore, we determined the threshold of the proportion of cells in the target outlets of uninfected samples as 7.10%.

The Reynolds number is affected by the flow rate, which influences the particle sorting efficiency (Amini et al., 2014). We demonstrated

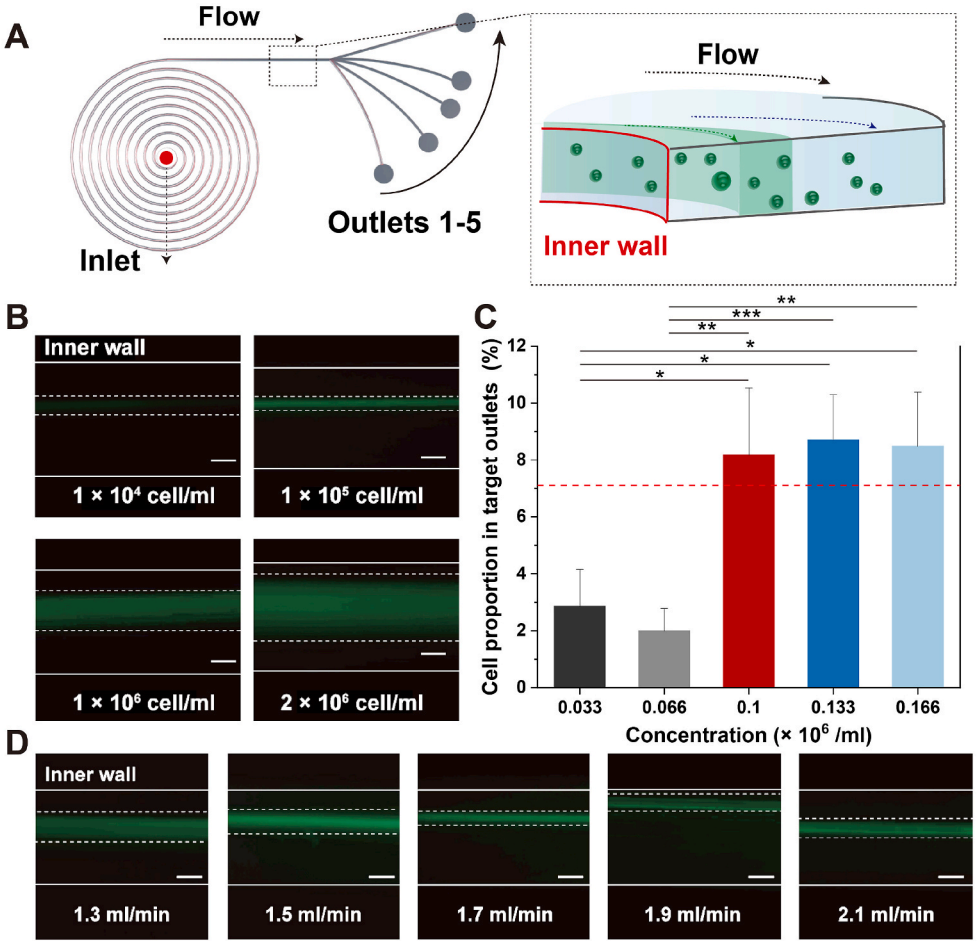

Fig. 3. Evaluation of operating parameters with the MIP device platform. A) Schematic of the optimization process. B) Representative images of Calcein AM stained monocytes under different cell concentrations (1 × 10^4 cells ml^{-1}, 1 × 10^5 cells ml^{-1}, 1 × 10^6 cells ml^{-1}, and 2 × 10^6 cells ml^{-1}). White dotted lines denoted the focused bandwidths of cells. Scale bar = 100 μm. C) The proportion of cells within target outlets 4–5 for samples with different monocyte concentrations. The threshold for the proportion of cells in target outlets of uninfected samples was determined as 7.10%. D) Representative images of Calcein AM stained monocytes under different flow rates (1.3 ml min^{-1}, 1.5 ml min^{-1}, 1.7 ml min^{-1}, 1.9 m min^{-1}, and 2.1 ml min^{-1}). Scale bar: 100 μm. * states for p values of <0.01, ** states for p values of <0.001, *** states for p values of <0.0001.

that as the flow rate increased, the focused bandwidth and equilibrium position of the cells were affected (Fig. 3D). Specifically, at lower flow rates (<1.7 ml min^{-1}), the focused bandwidth across the channel cross-section would be more diffused (1.3 ml min^{-1}: 101.53 ± 2.39 μm, 1.5 ml min^{-1}: 57.52 ± 1.31 μm) (Fig. 3D). The cell bandwidth obtained at a flow rate of 1.7 ml min^{-1} was consistently focused within the range of 25.5 ± 0.90 μm. At flow rates >1.7 ml min^{-1}, the equilibrium position of the focused bandwidth would also fluctuate and shift closer to the inner wall of the device channel. Therefore, we used a flow rate of 1.7 ml min^{-1} in our subsequent experiments to ensure cell focusing and separation consistency.

Due to the brief passage of cells through the MIP device platform, we hypothesized that the shear stress experienced by the cells during the enrichment process was negligible. To evaluate this, we analyzed the viability and morphology of the cells before and after enrichment using Calcein-AM dyes. We demonstrated no significant difference in the viability of monocytes before and after sorting (>93% viability; Fig. 4A). The cell morphology was also largely conserved with no visible physical changes or aberrations to cell viability (Fig. 4B), which indicated that the shear stress on the cells during processing was negligible.

Next, we showed that single bacteria would not be subjected to differential forces in the channel because the differences in size and deformability were negligible. We employed a *P. aeruginosa* strain engineered to constitutively produce the green fluorescent protein (GFP) for convenient observation and confirmation of our findings (Mok et al., 2020). GFP expression was used to verify the presence of infection and validate the MOI (Fig. 4C). We found that fluorescence readings above 1.01 reflected the presence of monocytes infected with *gfp*-tagged bacteria. Using the fluorescence intensity threshold value of uninfected monocytes (1.01; Supplementary Figure 4A), we determined that the average fluorescence intensity of a single *P. aeruginosa* bacterium was 1.56 ± 0.07 arbitrary unit (A.U). As shown by the quantification of colony-forming units (CFU), we found that the extracellular bacteria were evenly distributed across the device outlets (Supplementary Figure 4B). Therefore, the MOI of a sample could also be estimated based on the difference between the CFU counts obtained from Outlets 2–3 and the averaged CFU count obtained from samples of Outlets 1–5.

2.4. Label-free detection of low-level infections based on the presence of infected monocytes

After sorting the bacteria-internalized monocytes, we aim to validate the MIP platform for detecting low-level infections without the need for biomarker labeling. We first quantified the bacteria-internalized monocytes sorted to each outlet of the MIP device platform to determine the recovery rate and sorting efficiency of these monocytes from the uninfected populations. Then, the actual MOI was determined by dividing the total fluorescence intensity of monocytes by the average fluorescence intensity of an individual bacterium (1.56 A.U., Supplementary Figure 4A) monocyte count. For the convenience of labeling infection severity, samples of varying MOIs were classified into two degrees of infection, higher (0.1:1 to 1:1) and lower (0.01:1 to 0.1:1) infection rates (Supplementary Fig. 1A-D) (Francis and Thomas, 1996).

We demonstrated that samples with a higher proportion of infected monocytes due to higher infection rate (MOI 0.1:1 to 1:1) led to a lower average proportion of cells in the target outlets (Outlets 4 and 5) than the lower infection rate samples (reduction by 3.52 times) (Fig. 5A, Supplementary Fig. 5A and B). Compared with the uninfected controls, samples at a lower infection rate (MOI 0.01:1 to 0.1:1) also had a lower average proportion of cells at the target outlets (reduction by 1.46 times). For samples infected at MOI >0.1:1, the threshold of the proportion of cells in target outlets was 4.50%. The stiffer cells were more concentrated in Outlets 2 and 3 (Supplementary Fig. 5C and D), as shown by CFU count. The distinct thresholds demonstrated with higher and lower infection rate samples showed that the MIP device platform could identify positively infected samples and distinguish samples infected at various degrees of infection.

2.5. The MIP platform can detect infections from different bacterial species

To demonstrate the applicability of the MIP device for various bacterial infections, we also evaluated the proportion of cells in target outlets with samples infected by *Staphylococcus aureus* (*S. aureus*) (representing the most common Gram-positive bacterial pathogen) and *S. enterica* serovar Typhimurium (*S*. Typhimurium; representing the classical intracellular pathogen with the ability to survive intracellularly of monocytes). As demonstrated similarly with single *P. aeruginosa* cells

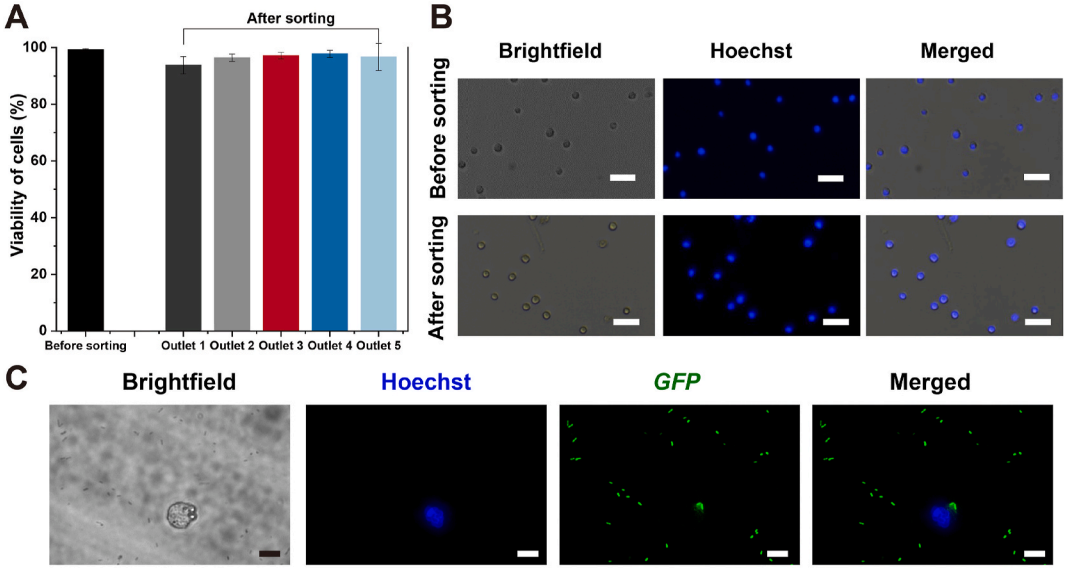

Fig. 4. Characterisation of monocytes and bacteria for disease detection. A) Cell viability of monocytes before and after sorting. No significant difference in cell viability was observed. B) Morphology of cells before (above) and after (below) sorting. Scale bar: 50 μm. C) Representative images of *gfp*-tagged *P. aeruginosa* and monocytes Scale bar: 10 μm.

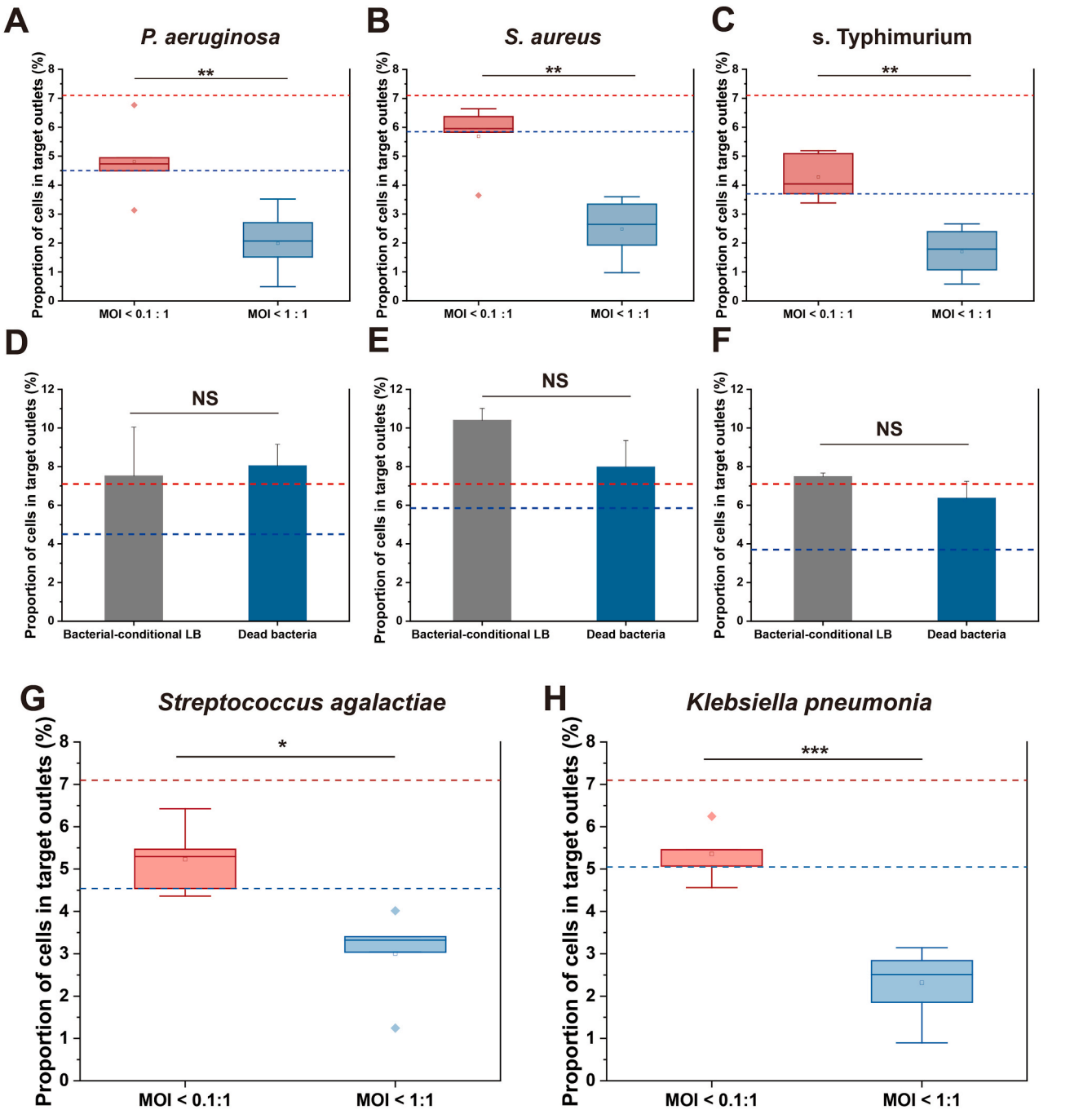

Fig. 5. Detection of infection based on the proportion of cells in target outlets. The proportion of cells in target outlets for samples infected at MOI <0.1:1 and < 1:1 with A) *P. aeruginosa* (p-value: 0.000695) and B) *S. aureus* (p-value: 0.00072) and C) *S.* Typhimurium (p-value = 0.001317). The thresholds of uninfected samples (7.10%) andsamples infected at MOI < 0.1:1 (*P. aeruginosa:* 4.50%; *S. aureus:* 5.85%; *S.* Typhimurium*:* 3.70%) were denoted by the dotted red and blue lines, respectively. The proportion of cells in target outlets for samples exposed to media conditioned by bacterial cultures or exposed to dead bacteria using D) *P. aeruginosa*, E) *S. aureus* or F) *S.* Typhimurium. The resultant proportion of cells in target outlets for each control was comparable to that obtained with healthy samples. The proportion of cells in target outlets for samples infected at MOI <0.1:1 and < 1:1 with G) *S. agalactiae* (p-value: 0.002526) and H) *K. pneumoniae* (p-value: 0.0000053). The thresholds of uninfected samples (7.10%) andsamples infected at MOI < 0.1:1 (*S. agalactiae*: 4.54%, *K. pneumoniae*: 5.05%) were denoted by the dotted red and blue lines, respectively. NS = not significant. * states for p values of <0.01, ** states for p values of <0.001, *** states for p values of <0.0001. (For interpretation of the references to colour in this figure legend, the reader is referred to the Web version of this article.)

(Supplementary Figure 4B*)*, even distribution of single *S. aureus* and *S.* Typhimurium cells were observed (Supplementary Figure 6). Expectedly, monocytes infected with *S. aureus* or *S.* Typhimurium led to similar modifications in their physical properties compared to uninfected monocytes (i.e., size and stiffness) (Supplementary Figure 7; Supplementary Figure 8).

For bacteria-infected samples, infected monocytes were similarly concentrated within Outlets 2–3 due to the higher flow rate within these channels (Supplementary Figure 9). The average fluorescence intensity of a single *S. aureus* bacterium was 1.25 ± 0.1 A.U (Supplementary Figure 4A). As with samples infected with *P. aeruginosa,* the stiffer cells infected with *S.* Typhimurium was more concentrated in Outlets 2 and 3, as shown by the CFU count (Supplementary Figure 10). We determined that the thresholds of cell proportion within the target outlets for

S. aureus and *S.* Typhimurium samples infected at lower MOI (>0.1:1) were 5.85% and 3.70%, respectively (Fig. 5B–C). Similar to *P. aeruginosa*, distinct thresholds of cells within target outlets infected at higher MOI (>1:1) could be obtained with samples infected by *S. aureus* (2.00%) and *S.* Typhimurium (1.08%). Interesting, we were able to distinguish samples infected with *S.* Typhimurium with even lower infection rates than those infected with *P. aeruginosa* or *S. aureus* (4.58 ± 0.45%, MOI 0.01:1), probably due to the intracellular nature of *S.* Typhimurium (Supplementary Figure 11).

We further hypothesized that internalized viable bacteria were required for a positive readout with the MIP device (Fig. 5D–F). To validate this, we quantified the proportion of cells obtained from a series of controls, using samples infected with *P. aeruginosa, S. aureus,* and *S.* Typhimurium. We first demonstrated that dead cells did not affect the overall distribution of cells at the outlets and that the proportion of dead cells in each outlet was evenly distributed (Supplementary Figure 12). We further demonstrated that in the absence of internalized viable bacteria, monocytes incubated with untreated LB media (8.59 ± 1.24%) were comparable to that of uninfected samples (Supplementary Figure 13). Besides, samples activated by conditioned media from bacterial cultures (*P. aeruginosa:* 7.51 ± 2.53%; *S. aureus:* 10.40 ± 0.62%; *S.* Typhimurium*:* 7.48 ± 0.18%) or treated with heat-deactivated bacteria (*P. aeruginosa:* 8.04 ± 1.11%; *S. aureus:* 7.98 ± 1.37%; *S.* Typhimurium*:* 6.36 ± 0.87%) did not lead to significant differences in cell proportion within target outlets compared to that of uninfected samples (Fig. 5D–F, Supplementary Figure 14). Furthermore, in these control samples, the proportion of cells within target outlets was also significantly higher than the 4.5% threshold previously established for samples infected at MOI >0.1: 1. These observations confirmed that only the internalization of viable bacteria by monocytes would generate a positive outcome.

To further validate the MIP platform for detection of bacterial infection with liquid (blood) biopsy, two other bacterial species commonly associated with BSIs, *Streptococcus agalactiae (S. agalactiae)* and *Klebsiella pneumoniae* (*K. pneumoniae*), were used (Orsini et al., 2012). We first demonstrated that the even distribution of single *S. agalactiae* and *K. pneumoniae* cells from each outlet (Supplementary Figure 15). Then, as supported by the CFU count, in samples infected with *S. agalactiae* and *K. pneumoniae*, infected stiffer monocytes will focus on Outlets 2–3, as similarly demonstrated previously with samples infected with *S. agalactiae* and *K. pneumoniae* (Supplementary Figure 16, 17). We further determined the distinct thresholds of monocytes in the target outlets for samples infected with *S. agalactiae* and *K. pneumoniae.* The threshold for samples infected with *K. pneumoniae* at low (>0.1:1) and high (>1:1) MOIs were 4.54% and 3.04%, and for samples infected

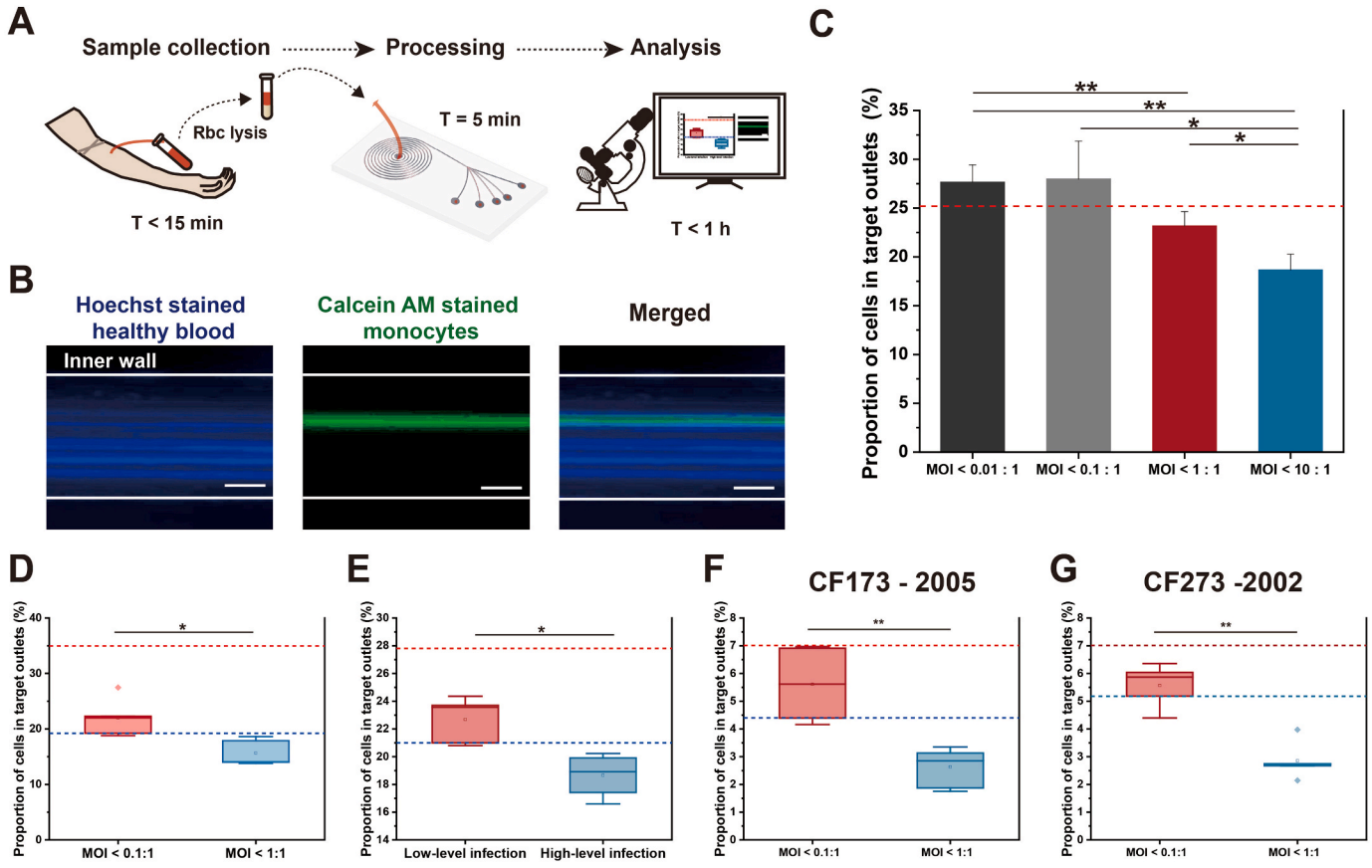

Fig. 6. Validation of clinical utility with blood samples and patient-derived clinical isolates. A) Schematic of clinical validation. B) Representative images of Calcein AM stained monocytes and Hoechst stained white blood cells in clinical samples. Scale bar: 100 μm. C) The proportion of cells for whole blood samples with spiked monocytes infected at MOI = 0.01:1, MOI = 0.1:1, MOI = 1:1 and MOI = 10:1. The dotted red line (25.21%) indicated the proportion of uninfected samples. D) The proportion of cells in target outlets for neutrophil-rich samples from whole blood infected at MOI <0.1:1 and < 1:1 with *P. aeruginosa.* The thresholds for uninfected healthy blood samples (34.96%) and neutrophil-rich samples infected at MOI < 0.1:1 (19.22%) were denoted by the dotted red and blue lines, respectively. E) The proportion of cells in target outlets for uninfected whole blood samples with spiked monocytes at low infection and high infection rates. The thresholds for samples of low infection rates (27.81%) and high infection rates (21.00%) were denoted by the dotted red and blue lines, respectively. The proportion of cells in target outlets for samples infected at MOI <0.1:1 and < 1:1 with F) CF173-2005 (p-value: 0.000983) and G) CF273-2002 (p-value: 0.000371). The thresholds of uninfected samples (7.10%) andsamples infected at MOI < 0.1:1 (CF173-2005: 4.40%, CF273-2002: 5.18%) were denoted by the dotted red and blue lines, respectively. * states for p values of <0.01, ** states for p values of <0.001. (For interpretation of the references to colour in this figure legend, the reader is referred to the Web version of this article.)

with *S. agalactiae* at low and high MOIs were 5.05% and 1.85%, respectively (Fig. 5G–H).

2.6. Validation of the MIP platform with spiked human blood samples

We aimed to demonstrate the clinical potential of the MIP device using small amounts of liquid (blood) biopsy, which is ideal for the routine monitoring of patients. Whole blood constitutes a variety of cells, including red blood cells (RBCs), platelets, neutrophils (70–80%) (Rosales, 2018), and leukocytes (Dean and Dean, 2005), among which monocytes account for 4.5–11 $\times$ 10^6 cells ml^{-1} in the blood (Dean and Dean, 2005). In addition, due to the presence of other phagocytic blood cells, the actual degree of infection simulated with these samples would be lower than the MOI used. Therefore, the threshold of the proportion of cells obtained at the target outlets could vary from patient to patient.

We first used whole blood samples processed briefly with an RBC lysis buffer to obtain the nucleated cell fraction comprising neutrophil-rich populations (Fig. 6A). We demonstrated that the proportion of cells in the target outlets (Outlets 4–5) was higher with healthy blood controls than the threshold previously established with pure monocyte samples (34.96 $\pm$ 1.70%, Supplementary Figure 18), suggesting the presence of other phagocytic cells. This observation was also likely attributed to larger WBCs in the nucleated cell fraction, which confirmed the importance of determining a personalized threshold for clinical utility.

To determine if other types of WBCs, such as neutrophils, could internalize bacteria and affect the sorting efficacy of the MIP platform, we utilized the RBC-lysed neutrophil-rich population for subsequent bacterial infection. Similar to monocyte-based assays, *gfp*-tagged *P. aeruginosa* was used to infect the neutrophil-rich population for 2 h, and the actual MOI was determined based on the average fluorescence intensity of an individual bacterium (1.56 A.U., Supplementary Figure 4A). We demonstrated that the proportion of cells in target outlets was expectedly reduced in the presence of infection for neutrophil-rich samples infected at MOI 0.1:1 to 1:1 (Supplementary Figure 19). As described previously, the threshold to distinguish between infected and uninfected samples was 34.96% (Fig. 6C, Supplementary Figure 18). For samples infected at MOI >0.1:1, the threshold of the proportion of cells in target outlets was 19.22% (Fig. 6D).

Next, we screened blood samples spiked with clinically relevant proportions (Bedi et al., 2016; Shin et al., 2017) of bacteria-internalized monocytes (Supplementary Figure 20). Cell concentrations corresponding to infected monocyte fractions in blood were prepared to fit our predetermined optimal cell concentration range (0.1–1 $\times$ 10^6 cells per ml, Fig. 3B–C, Fig. 6B). For samples spiked with uninfected monocytes, the proportion of cells in target outlets was also higher than that of the pure monocyte samples (25.21 $\pm$ 2.95%, Supplementary Figure 21).

Due to the heterogeneity of blood composition in patients, we hypothesized that a personalized threshold could be obtained by determining the threshold baseline obtained for each clinical sample. To demonstrate the establishment of a personalized threshold, monocytes infected at various MOIs (10:1, 1:1, 0.1:1, and 0.01:1) were spiked into lysed blood samples. We demonstrated that the serially diluted samples spiked with monocytes infected various MOIs resulted in a gradient of thresholds of the proportion of cells in the target outlets (Fig. 6C). Diluted samples corresponding to the lowest MOI (0.1:1 and 0.01:1) resulted in a negligible difference between the proportion of cells in the target outlet, indicating that a personalized baseline value could be obtained from the average of thresholds from these dilutions (27.81%), allowing clinicians to predict the presence of infection for the patient. The same blood sample spiked with different amounts of infected monocytes corresponding to a high (MOI 10:1) and low-level of infections (MOI 1:1) led to distinct thresholds of 21.00% and 27.81%, respectively (Fig. 6E, Supplementary Figure 22), which reflects the importance of a personalized threshold for individual patients.

2.7. Clinical validation of the MIP platform with patient-derived isolates

It is important to evaluate the potential of the MIP device for clinical utility. Specifically, we aimed to incorporate the MIP device in the routine screening of patients to detect infections early. The device was validated with clinical isolates from cystic fibrosis patients with *P. aeruginosa*-based pneumonia (n = 2). Similar to the laboratory cultured strains, clinical isolates of *P. aeruginosa* (CF173-2005 and CF273-2002) (Chua et al., 2016a) were used to infected monocytes, and the proportion of cells in target outlets after infection were evaluated.

We first confirmed that single bacteria were uniformly distributed for patient-derived clinical isolates as with the previous prototypic *P. aeruginosa* samples (Supplementary Figure 23). Using CFU data, we subsequently confirmed that the infected stiffer monocytes were more concentrated in the target outlets 2–3 (Supplementary Figure 24, 25). At low (MOI > 0.1:1) and high (MOI > 1:1) infection rates for CF173-2005, the threshold of the proportion of cells in the target outlets was 4.40% and 1.87%, respectively (Fig. 6F). Similar to CF173-2005, the thresholds of cell proportion in the target outlets at lower MOI (>0.1:1) and higher MOI (>1:1) for CF273-2002 were 5.18% and 2.67%, respectively (Fig. 6G). Therefore, we clearly demonstrated the potential clinical utility of the MIP platform for the personalized management of the infectious disease. These screens with patient-derived clinical samples highlighted the potential of this technology in personalized management for infectious disease, reflecting a consistent efficiency rate and utility of the device for clinical applications. Hence, the MIP device applications are versatile and have far-reaching implications for various clinical settings.

3. Discussion

Diagnosing asymptomatic cases or infections with mild symptoms is a significant challenge caused by early-stage or intracellular bacterial infections. As bacteria can hide in host cells and evade recognition by the immune system, false-negative readings in routine culture assays are common (Mickiewicz et al., 2019; Tuchscherr et al., 2011). Furthermore, as clinicians usually have a narrow treatment window, any treatment delay will increase disease severity and mortality (Chen et al., 2020; Lee et al., 2007). This warrants the imperative need to develop a rapid, sensitive diagnosis method to detect such infections.

Here, we presented a label-free microfluidic-based phagocytosis biosensor to diagnose infections by rapidly detecting rare bacteria-internalized monocytes from non-infected host cells for detection, based on increased size and stiffness of monocytes with internalized bacteria. The MIP microfluidic platform required only simple optical imaging to generate outputs that identify infection and provide readouts within 1.5 h. Because of its ease of operations and low fabrication cost, clinicians could screen many samples in parallel under high throughput with minimal equipment requirements to identify immunocompromised individuals with potential risks of worsening infection, thereby facilitating early treatment interventions. Moreover, the optimal cell concentration required also corresponded to only a small blood sample volume (~1 ml), thus enabling routine screening and POC detection. We also confirmed that the MIP platform was applicable to a wide range of pathogens and present as a phagocytosis detection platform that could benefit the early detection of infectious diseases, including patients with BSIs.

Overall, we leveraged our novel findings in the mechanics of bacteria-internalized phagocytes to develop a robust and novel strategy to detect low-level or intracellular infections caused by different bacterial species. We envision that our proof-of-concept MIP device platform could be conveniently translated to other infections, including those caused by fungi and parasites.

4. Experimental section

4.1. Bacteria and monocyte cell cultures

P. aeruginosa PAO1, *S. aureus* 15981, *S. enterica* serovar Typhimurium ATCC14028, *S. agalactiae* COH1, and *K. pneumoniae* KP-1 were cultured in 2 ml Luria-Bertani (LB) media (Becton, Dickinson and Company, #244620, USA) at 37 °C overnight, where bacteria concentrations would reach approximately 10^9 cells ml^{-1} (Liu et al., 2021). Bacteria suspensions were centrifuged at 11.8×10^3 RCF for 3 min and resuspended in 1 ml PBS. As previously reported, *gfp*-tagged *P. aeruginosa* and *gfp*-tagged *S. aureus* were used to visualize the infection of bacteria (Chua et al., 2016b).

P. aeruginosa patient-derived clinical isolates used to validate the clinical utility of the platform were CF173-2005 isolate of lineage H and CF273-2002 of similar lineage, which was isolated from cystic fibrosis patients in Denmark (Yang et al., 2011).

Monocyte cell line (U937) was cultured in RPMI-1640 (Gibco, # 11875085, USA) supplemented with 10% FBS (Gibco, # 10270106, USA) and 1% penicillin-streptomycin (Gibco, # 15140122, USA). Cells were cultured in optimal conditions under a 5% CO_2 atmosphere at 37 °C under humidified conditions. Media were refreshed every 48 h, and cells were passaged at 80% confluence.

4.2. Infection assays

As previously described (Chua et al., 2014), monocytes were washed three times with phosphate buffer saline (PBS) (Gibco, # 70011044, USA) and transferred to the fresh RPMI-1640 medium + 10% PBS. Monocytes were infected with bacteria in RPMI-1640/10% FBS (no antibiotics added) at different MOI (10:1, 1:1, and 0.1:1, 0.01:1) and incubated at 37 °C under 5% CO_2, 99% humidity, for 2 h. Infected samples were centrifuged at 260 RCF for 3 min and resuspended in fresh cell culture media three times to remove unbound extracellular bacteria.

4.3. Device fabrication

The fabrication of the molds was performed by photolithography, as previously described (Zhang et al., 2021). The aluminum mold was fabricated by micromachining (Deng et al., 2021; Khoo et al., 2019). Patterns were replicated from the mold using polydimethylsiloxane (PDMS) base (SYLGARDTM 184 Silicone Elastomer kit, Germany) by mixing the polymer with the curing agent at a ratio of 10:1. The PDMS was cured in an oven at 60 °C for 2 h after degassing with a vacuum pump. After curing, the PDMS layer was gently peeled off from the aluminum mold. A 5 min plasma treatment bonded PDMS layers, and the device was assembled in the oven at 80 °C for another 2 h. The channel width of the device was 500 μm, and the height was 200 μm at the inner and outer walls of the channel, respectively. The width of each of the five outlets was 100 μm. The length of the main straight channel is 15 mm, while the length for each of the outlets is 10 mm.

For the cell deformability device, a silicon wafer was coated with protective photoresist AZ5214 (AZ Electronic Materials, Wiesbaden, Germany), followed by UV exposure. The developed silicon wafer with photoresist was then etched by deep reactive-ion etching (DRIE). After removing the protective photoresist using acetone, the etched silicon wafer was treated with silane (Sigma-Aldrich, St. Louis, MO).

4.4. Device processing

Bonded devices were assessed for leakage before use. Samples were resuspended in 1.5 ml PBS and introduced to the MIP device platform at a flow rate of 1.7 ml min^{-1}, using a syringe pump (New Era Pump System, Inc, USA). Cells were collected from each outlet in 1.5 ml tubes.

4.5. Cell viability and immunostaining

Monocytes were stained with 5 μM Hoechst (for nuclei labeling), Calcein AM (Invitrogen, #C3100MP, USA) and 5 μM Propidium Iodide (PI) (Sigma-Aldrich, #81845, USA) respectively, and incubated under 37 °C for 30 min (Calcein AM), room temperature for 1 min (PI) to identify live and dead cells. Samples were washed with PBS before fluorescence imaging with a fluorescence microscope (Nikon, Eclipse Ci-L, Japan).

4.6. Stiffness measurement

Cell stiffness of the monocytes was quantified by our previously developed elasticity microcytometer (Hu et al., 2016). Before the stiffness measuring experiments, the device was coated with 1% (w/w) pluronic F-127 (Sigma-Aldrich, P2443, USA) for 30 min to prevent cell adhesion. The cells were briefly injected with a steady driving pressure into confining microchannels with confining channels. The cells were trapped at a confining channel position where the channel width is narrow enough to trap the cells under the driving pressure. Micrographs of the confining channels with the trapped cells were captured under a phase-contrast inverted microscope (Nikon, Eclipse Ci-L, Japan) at 100 Pa pressure. The cell elasticity was determined by the cell size and position in the confining microchannel obtained from the micrographs. The elastic modulus of monocytes was then calculated based on the hyperelastic Tatara model, as shown in Equation (2) (Hu et al., 2018; Ren et al., 2020):

$$E = \frac{3(1-\nu^2)A}{2(D_{cell}-W_{deform})}\left(1+\frac{2Ba^2}{D_{deform}^2}\right)\frac{F_{compress}}{a} - \frac{2A}{\pi(D_{cell}-W_{deform})}\left(1+\frac{4Ba^2}{5D_{deform}^2}\right)\frac{F_{compress}}{f(a)} \quad (2)$$

Where D_{cell} is the cell diameter, D_{deform} is the deformed cell diameter, W_{deform} is the deformed cell width, ν is the Poisson's ratio of a cell, a is the contact radius, and $f(a)$ is the characteristic length of the non-spherical geometry after deformation.

A and B in the above equation can be given as (3),

$$A = \frac{(1-\xi)^2}{1-\xi+\frac{\xi^2}{3}}, B = \frac{1-\frac{\xi}{3}}{1-\xi+\frac{\xi^2}{3}}, \xi = 1-\frac{W_{deform}}{D_{cell}} \quad (3)$$

Where ξ is the deformation of the cell.

4.7. Colony-forming unit (CFU) assay

As previously described (Chan et al., 2020), bacterial suspensions were collected and serially diluted for growth on an LB agar plate (Sigma-Aldrich, #L3027, USA) at 37 °C for 24 h to quantify bacterial counts. The CFU mL^{-1} was obtained by the average number of colonies × dilution factor × volume. The data obtained from the infection assay were normalized by dividing the average CFU value of outlets 1 and 5.

4.8. Control assays with activated monocytes

Activated monocytes were obtained by treating naïve monocytes with 0.22-μm filter-sterilized LB media conditioned with live bacteria for 2 h or exposure to heat-deactivated bacteria (MOI 10:1).

4.9. Whole blood test

Single donor human whole blood (Innovative Research, Inc, #IWB1K2E10ML, USA) was mixed with RBC lysis buffer (1:9 ratio, Invitrogen, # 00-4333-57, USA) and shaken gently for 5 min. Lysed samples were centrifuged at 500×*g* for 5 min. RBC debris and plasma

were discarded, and the remaining WBC pellet was resuspended into 1 ml PBS for further use.

For infection assays, infected samples at MOI = 10: 1, MOI = 1: 1 were obtained by spiking infected monocytes into blood samples after RBC lysis, followed by direct processing with the device.

For neutrophil-rich population infection assays, the neutrophil-rich population was infected with *P. aeruginosa* at different MOIs (0.1:1 and 1:1). The count of bacteria was determined by multiplying the experimental MOI rate and the cell count.

4.10. Imaging and analysis

Cell suspensions were collected from each outlet for imaging under a fluorescent microscope. Cells were resuspended in the 1.5 ml tube, and an 18 well plate (Ibidi, #81826, Germany) was used to place the mixed cell suspension. The nuclei of cells were stained by 5 μM Hoechst (Invitrogen, #H1399, USA) to quantify cell recovery and cell proportions within outlets. Images of monocytes with and without internalized pathogens were obtained to characterize the cell size before and after infection, and the cell size was quantified with predetermined algorithms. All fluorescent images were processed by Image J software (National Institutes of Health, USA). Automated algorithms were used to establish cell counts and quantify intensity outputs. Fluorescent intensity was normalized to background intensity values. Data were plotted by Origin software (OriginLab Corporation, USA).

4.11. Statistical analysis

The results were expressed as means ± standard deviation. Data groups were compared using the one-way ANOVA and Student's t-test to evaluate associations between independent variables, and the P values were obtained. Three independent trials were conducted in triplicates for each experiment.

Funding

Research Grants Council (RGC 9610430 and 11204317); City University of Hong Kong, Hong Kong Polytechnic University (BE2B); Environmental and Conservation Fund (ECF 49/2019) and State Key Laboratory for Chemical Biology and Drug Discovery (1-BBX8).

Author contributions

Conceived and designed the experiments: BLK, SLC, JCL. Performed the experiments: JCL, JFR. Analyzed the data: BLK, SLC, JCL. Contributed reagents/materials/analysis tools: BLK, SLC, RCHW. Wrote the paper: BLK, SLC, JFR, RCHW, JCL. All authors have read the manuscript.

Data and materials availability

All data needed to evaluate the conclusions in the paper are present in the paper and/or the Supplementary Materials.

Declaration of competing interest

The authors declare the following financial interests/personal relationships which may be considered as potential competing interests: One or more authors have a pending patent related to this work.

Acknowledgments

This study was supported by the Research Grants Council (RGC). This work was also supported by the City University of Hong Kong (9610430) and the Hong Kong Polytechnic University, Department of Applied Biology and Chemical Technology Startup Grant (BE2B), State Key Laboratory of Chemical Biology and Drug Discovery Fund (1-BBX8) and Environment & Conservation Fund (ECF 48/2019).

Acronyms

MIP	Monocytes with internalized pathogens
BSIs	Bloodstream infections
WBCs	White blood cells
P. aeruginosa	*Pseudomonas aeruginosa*
MOI	Multiplicity of infection
F_L	Inertial lift force
F_D	Dean Drag force
F_{LD}	Lift force induced by deformability
GFP	Green fluorescent protein
CFU	Colony-forming units
S. aureus	*Staphylococcus aureuss*
S. Typhimurium	*S. enterica* serovar Typhimurium
S. agalactiae	*Streptococcus agalactiae*
K. pneumoniae	*Klebsiella pneumoniae*
RBCs	Red blood cells
A.U	Arbitrary unit

Appendix A. Supplementary data

Supplementary data to this article can be found online at https://doi.org/10.1016/j.bios.2021.113412.

References

Amini, H., Lee, W., Di Carlo, D., 2014. Inertial microfluidic physics. Lab Chip 14 (15), 2739–2761.
Bedi, B., Yuan, Z., Joo, M., Zughaier, S.M., Goldberg, J.B., Arbiser, J.L., Hart, C.M., Sadikot, R.T., 2016. Enhanced clearance of Pseudomonas aeruginosa by peroxisome proliferator-activated receptor gamma. Infect. Immun. 84 (7), 1975–1985.
Blauwkamp, T.A., Thair, S., Rosen, M.J., Blair, L., Lindner, M.S., Vilfan, I.D., Kawli, T., Christians, F.C., Venkatasubrahmanyam, S., Wall, G.D., 2019. Analytical and clinical validation of a microbial cell-free DNA sequencing test for infectious disease. Nat. Microbiol. 4 (4), 663–674.
Buyck, J.M., Tulkens, P.M., Van Bambeke, F., 2013. Pharmacodynamic evaluation of the intracellular activity of antibiotics towards Pseudomonas aeruginosa PAO1 in a model of THP-1 human monocytes. Antimicrob. Agents Chemother. 57 (5), 2310–2318.
Chan, S.Y., Liu, S.Y., Seng, Z., Chua, S.L., 2020. Biofilm matrix disrupts nematode motility and predatory behavior. ISME J. 15 (1), 260–269.
Chen, C.K., Liao, J., Li, M.S., Khoo, B.L., 2020. Urine biopsy technologies: cancer and beyond. Theranostics 10 (17), 7872–7888.
Chua, S.L., Ding, Y., Liu, Y., Cai, Z., Zhou, J., Swarup, S., Drautz-Moses, D.I., Schuster, S. C., Kjelleberg, S., Givskov, M., Yang, L., 2016a. Reactive oxygen species drive evolution of pro-biofilm variants in pathogens by modulating cyclic-di-GMP levels. Open Biol. 6 (11), 160162.
Chua, S.L., Liu, Y., Yam, J.K.H., Chen, Y., Vejborg, R.M., Tan, B.G.C., Kjelleberg, S., Tolker-Nielsen, T., Givskov, M., Yang, L., 2014. Dispersed cells represent a distinct stage in the transition from bacterial biofilm to planktonic lifestyles. Nat. Commun. 5 (1), 4462.
Chua, S.L., Yam, J.K.H., Hao, P., Adav, S.S., Salido, M.M., Liu, Y., Givskov, M., Sze, S.K., Tolker-Nielsen, T., Yang, L., 2016b. Selective labelling and eradication of antibiotic-tolerant bacterial populations in Pseudomonas aeruginosa biofilms. Nat. Commun. 7 (1), 1–11.
Conzelmann, C., Gilg, A., Gross, R., Schutz, D., Preising, N., Standker, L., Jahrsdorfer, B., Schrezenmeier, H., Sparrer, K.M.J., Stamminger, T., Stenger, S., Munch, J., Muller, J. A., 2020. An enzyme-based immunodetection assay to quantify SARS-CoV-2 infection. Antivir. Res. 181, 104882.
Dean, L., Dean, L., 2005. Blood Groups and Red Cell Antigens. NCBI, Bethesda, Md, USA.
Deng, Y., Liu, S.Y., Chua, S.L., Khoo, B.L., 2021. The effects of biofilms on tumor progression in a 3D cancer-biofilm microfluidic model. Biosens. Bioelectron. 180, 113113.
Francis, M.S., Thomas, C.J., 1996. Effect of multiplicity of infection on Listeria monocytogenes pathogenicity for HeLa and Caco-2 cell lines. J. Med. Microbiol. 45 (5), 323–330.
Garai, P., Berry, L., Moussouni, M., Bleves, S., Blanc-Potard, A.B., 2019. Killing from the inside: intracellular role of T3SS in the fate of Pseudomonas aeruginosa within macrophages revealed by mgtC and oprF mutants. PLoS Pathog. 15 (6), e1007812.
Garcia-Medina, R., Dunne, W.M., Singh, P.K., Brody, S.L., 2005. em>Pseudomonas aeruginosa acquires biofilm-like properties within airway epithelial cells. Infect. Immun. 73 (12), 8298–8305.
Gossett, D.R., Tse, H.T., Lee, S.A., Ying, Y., Lindgren, A.G., Yang, O.O., Rao, J., Clark, A. T., Di Carlo, D., 2012. Hydrodynamic stretching of single cells for large population mechanical phenotyping. Proc. Natl. Acad. Sci. U. S. A. 109 (20), 7630–7635.

Guzniczak, E., Otto, O., Whyte, G., Willoughby, N., Jimenez, M., Bridle, H., 2020. Deformability-induced lift force in spiral microchannels for cell separation. Lab Chip 20 (3), 614–625.
Herrmann, N., Neubauer, P., Birkholz, M., 2019. Spiral microfluidic devices for cell separation and sorting in bioprocesses. Biomicrofluidics 13 (6), 061501.
Hu, S., Liu, G., Chen, W., Li, X., Lu, W., Lam, R.H., Fu, J., 2016. Multiparametric biomechanical and biochemical phenotypic profiling of single cancer cells using an elasticity microcytometer. Small 12 (17), 2300–2311.
Hu, S., Wang, R., Tsang, C.M., Tsao, S.W., Sun, D., Lam, R.H., 2018. Revealing elasticity of largely deformed cells flowing along confining microchannels. RSC Adv. 8 (2), 1030–1038.
Kang, D.K., Ali, M.M., Zhang, K., Huang, S.S., Peterson, E., Digman, M.A., Gratton, E., Zhao, W., 2014. Rapid detection of single bacteria in unprocessed blood using Integrated Comprehensive Droplet Digital Detection. Nat. Commun. 5, 5427.
Khoo, B.L., Shang, M., Ng, C.H., Lim, C.T., Chng, W.J., Han, J., 2019. Liquid biopsy for minimal residual disease detection in leukemia using a portable blast cell biochip. NPJ Precis. Oncol. 3, 30.
Lee, A., Mirrett, S., Reller, L.B., Weinstein, M.P., 2007. Detection of bloodstream infections in adults: how many blood cultures are needed? J. Clin. Microbiol. 45 (11), 3546–3548.
Lim, E.J., Ober, T.J., Edd, J.F., Desai, S.P., Neal, D., Bong, K.W., Doyle, P.S., McKinley, G. H., Toner, M., 2014. Inertio-elastic focusing of bioparticles in microchannels at high throughput. Nat. Commun. 5, 4120.
Liu, S.Y., Leung, M.M.-L., Fang, J.K.-H., Chua, S.L., 2021. Engineering a microbial 'trap and release' mechanism for microplastics removal. Chem. Eng. J. 404, 127079.
Masters, T.A., Pontes, B., Viasnoff, V., Li, Y., Gauthier, N.C., 2013. Plasma membrane tension orchestrates membrane trafficking, cytoskeletal remodeling, and biochemical signaling during phagocytosis. Proc. Natl. Acad. Sci. Unit. States Am. 110 (29), 11875–11880.
Mickiewicz, K.M., Kawai, Y., Drage, L., Gomes, M.C., Davison, F., Pickard, R., Hall, J., Mostowy, S., Aldridge, P.D., Errington, J., 2019. Possible role of L-form switching in recurrent urinary tract infection. Nat. Commun. 10 (1), 4379.
Mok, N., Chan, S.Y., Liu, S.Y., Chua, S.L., 2020. Vanillin inhibits PqsR-mediated virulence in Pseudomonas aeruginosa. Food Funct. 11 (7), 6496–6508.
Orsini, J., Mainardi, C., Muzylo, E., Karki, N., Cohen, N., Sakoulas, G., 2012. Microbiological profile of organisms causing bloodstream infection in critically ill patients. J. Clin. Med. Res. 4 (6), 371.
Peker, N., Couto, N., Sinha, B., Rossen, J.W., 2018. Diagnosis of bloodstream infections from positive blood cultures and directly from blood samples: recent developments in molecular approaches. Clin. Microbiol. Infect. 24 (9), 944–955.
Peters, R.P., van Agtmael, M.A., Danner, S.A., Savelkoul, P.H., Vandenbroucke-Grauls, C. M., 2004. New developments in the diagnosis of bloodstream infections. Lancet Infect. Dis. 4 (12), 751–760.
Ren, J., Li, Y., Hu, S., Liu, Y., Tsao, S.W., Lau, D., Luo, G., Tsang, C.M., Lam, R.H., 2020. Nondestructive quantification of single-cell nuclear and cytoplasmic mechanical properties based on large whole-cell deformation. Lab Chip 20 (22), 4175–4185.
Rosales, C., 2018. Neutrophil: a cell with many roles in inflammation or several cell types? Front. Physiol. 9, 113.
Shen, H., Wang, J., Liu, H., Li, Z., Jiang, F., Wang, F.B., Yuan, Q., 2016. Rapid and selective detection of pathogenic bacteria in bloodstream infections with aptamer-based recognition. ACS Appl. Mater. Interfaces 8 (30), 19371–19378.
Shin, H., Jeon, J., Lee, J.H., Jin, S., Ha, U.H., 2017. Pseudomonas aeruginosa GroEL stimulates production of PTX3 by activating the NF-kappaB pathway and simultaneously downregulating MicroRNA-9. Infect. Immun. 85 (3).
Srivastava, N., Traynor, D., Piel, M., Kabla, A.J., Kay, R.R., 2020. Pressure sensing through Piezo channels controls whether cells migrate with blebs or pseudopods. Proc. Natl. Acad. Sci. Unit. States Am. 117 (5), 2506–2512.
Tuchscherr, L., Medina, E., Hussain, M., Volker, W., Heitmann, V., Niemann, S., Holzinger, D., Roth, J., Proctor, R.A., Becker, K., Peters, G., Loffler, B., 2011. Staphylococcus aureus phenotype switching: an effective bacterial strategy to escape host immune response and establish a chronic infection. EMBO Mol. Med. 3 (3), 129–141.
Yang, L., Jelsbak, L., Marvig, R.L., Damkiær, S., Workman, C.T., Rau, M.H., Hansen, S.K., Folkesson, A., Johansen, H.K., Ciofu, O., Høiby, N., Sommer, M.O.A., Molin, S., 2011. Evolutionary dynamics of bacteria in a human host environment. Proc. Natl. Acad. Sci. Unit. States Am. 108 (18), 7481–7486.
Yap, B., Kamm, R.D., 2005. Mechanical deformation of neutrophils into narrow channels induces pseudopod projection and changes in biomechanical properties. J. Appl. Physiol. 98 (5), 1930–1939.
Zhang, J., Chua, S.L., Khoo, B.L., 2021. Worm-based microfluidic biosensor for real-time assessment of the metastatic status. Cancers (Basel) 13 (4).
Zhou, Y., Ma, Z., Ai, Y., 2018. Sheathless inertial cell focusing and sorting with serial reverse wavy channel structures. Microsyst. Nanoeng. 4, 5.
Zhu, Y., Qiao, L., Prudent, M., Bondarenko, A., Gasilova, N., Moller, S.B., Lion, N., Pick, H., Gong, T., Chen, Z., Yang, P., Lovey, L.T., Girault, H.H., 2016. Sensitive and fast identification of bacteria in blood samples by immunoaffinity mass spectrometry for quick BSI diagnosis. Chem. Sci. 7 (5), 2987–2995.

Further Reading

Liu, S.Y., Leung, M.M.-L., Fang, J.K.-H., Chua, S.L., 2021. Engineering a microbial 'trap and release' mechanism for microplastics removal. Chem. Eng. J. 404, 127079.